ACS Catalysis

Research Article

pubs.acs.org/acscatalysis

Metal Phosphides Derived from Hydrotalcite Precursors toward the Selective Hydrogenation of Phenylacetylene

Yudi Chen,[†] Changming Li,[‡] Junyao Zhou,[†] Shitong Zhang,[†] Deming Rao,[†] Shan He,*[,†] Min Wei,*[,†] David G. Evans,[†] and Xue Duan[†]

[†]State Key Laboratory of Chemical Resource Engineering, Beijing University of Chemical Technology, Beijing 100029, P. R. China

[‡]State Key Laboratory of Multi-phase Complex Systems, Institute of Process Engineering, Chinese Academy of Sciences, Beijing 100190, China

Supporting Information

ABSTRACT: We report a new synthetic strategy for the fabrication of several supported nickel phosphides ($Ni_{12}P_5$, Ni_2P, and NiP_2) with particle size ranging from 5 to 15 nm via a two-step procedure: preparation of supported Ni particles from layered double hydroxide precursors, followed by a further reaction with a certain amount of red phosphorus. The selective hydrogenation of phenylacetylene over these metal phosphides was evaluated, and the as-prepared Ni_2P/Al_2O_3 catalyst shows a much higher selectivity to styrene (up to 88.2%) than $Ni_{12}P_5/Al_2O_3$ (48.0%), NiP_2/Al_2O_3 (65.9%), and Ni/Al_2O_3 (0.7%) catalysts. EXAFS and in situ IR measurements reveal that the incorporation of P increases the bond length of Ni−Ni, which imposes a key influence on the adsorption state of alkene intermediates: as the Ni−Ni bond length extends to 0.264 nm, the alkene intermediate undergoes di-π(C═C) adsorption, facilitating its desorption and the resulting enhanced selectivity. Moreover, electron transfer occurs from Ni to P, as confirmed by EXAFS, XPS, and in situ CO-IR experiment, in which the positively charged Ni reduces the desorption energy of alkene and thus improves the reaction selectivity.

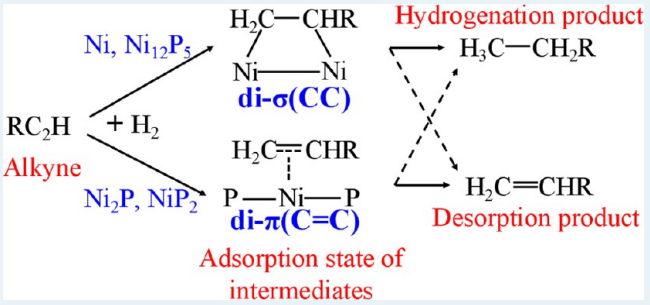

KEYWORDS: *metal phosphides, LDHs, selective hydrogenation, EXAFS, in situ IR*

1. INTRODUCTION

Metal phosphides[1] (MPs) are a class of intriguing materials with various compositions and ratios, which show fascinating properties in magnetic,[2] electronic,[3] and catalytic applications[4] due to their specific structure. Especially, their catalytic performances have attracted extensive research interest during the last decades. For instance, several studies have shown that transition metal phosphides (e.g., MoP, CoP, Fe_2P, and Ni_2P) display extremely high activity toward hydrodesulfurization (HDS) and hydrodenitrogeneration (HDN) reactions.[5] Moreover, Ni−P materials have recently been applied to the selective hydrogenation of alkyne with rather good performances.[6] For the preparation of metal phosphides, a number of synthetic approaches have been reported (e.g., solid-state reaction,[7] solvothermal reaction[8] and high temperature reduction of the oxide precursors);[9] however, these methods normally suffer from rigorous conditions, noxious organic reagents, or serious self-agglomeration of product in the reaction process. Therefore, the development of green and universal synthetic routes of metal phosphides with precisely controlled structure, composition, and particle size, so as to achieve tunable catalytic property, is highly desirable and remains a challenging goal.

Layered double hydroxides (LDHs) are a class of two-dimensional (2D) anionic clays consisting of positively charged host layers and exchangeable interlayer anions, which can be generally expressed by the formula $[M^{2+}_{1-x}M^{3+}_{x}(OH)_2]\text{-}(A^{n-})_{x/n}\cdot mH_2O$.[10] An unique structural characteristic of LDHs materials is that the M^{2+} and M^{3+} cations are distributed in a highly ordered manner in the hydroxide layers, as verified by Grey et al. by means of multinuclear NMR spectroscopy.[10c] Recently, supported metal nanoparticles derived from LDHs precursors have been reported as highly efficient catalysts based on the structural topotactic transformation of LDH materials upon calcination in a reductive atmosphere, which possess the unique properties of high dispersion (resulting from the atomic-scale dispersion of metal cations) as well as high stability (described as the anchoring effect of the substrate).[11,12] Inspired by the structural merits of LDHs materials, here we develop a new strategy for synthesizing supported metal phosphides: by using the immobilized metal nanoparticles derived from LDHs as "reactive seeds", a solid−gas reaction will occur via introducing another reactant (red phosphorus). The resulting supported metal phosphides inherit the high dispersion and stability of parent metal nanoparticles, and the

Received: March 30, 2015
Revised: August 21, 2015
Published: August 25, 2015

DOI: 10.1021/acscatal.5b01429
ACS Catal. 2015, 5, 5756−5765

chemical composition, structure, and morphology can be facilely controlled by tuning the reaction conditions and molar ratio of metal/red phosphorus.

In this work, three supported nickel phosphides ($Ni_{12}P_5$, Ni_2P, and NiP_2) on Al_2O_3 matrix with particle size range of 5−15 nm were prepared via a two-step procedure as mentioned above, and their catalytic performances toward selective hydrogenation of phenylacetylene were studied in detail. With the increase of P/Ni ratio, the activity of as-synthesized catalysts decreases gradually while the selectivity dramatically enhances. The Ni_2P/Al_2O_3 catalyst shows the best catalytic behavior with a conversion of 98.6% and selectivity of 88.2% (100 °C, 0.3 MPa, 3 h), which can serve as a promising candidate for the substitution of noble metal catalysts. The synthesis strategy demonstrated in this work takes the advantages of facile and benign preparation, good controllability in product structure and composition. In addition, a combination study based on experiment and DFT calculation reveals how the geometric and electronic effect influence the hydrogenation activity and selectivity, which gives a deep understanding on structure−function correlation and is helpful for new catalyst design and mechanism study.

2. EXPERIMENTAL SECTION

2.1. Materials. $Ni(NO_3)_2{\cdot}6H_2O$, $Al(NO_3)_3{\cdot}9H_2O$, $Fe(NO_3)_3{\cdot}9H_2O$, $Co(NO_3)_2{\cdot}6H_2O$, $Mg(NO_3)_2{\cdot}6H_2O$, urea, NH_4F, red phosphorus, 2-propanol and phenylacetylene were purchased and used without further purification. Deionized water was used in all the experimental processes.

2.2. Synthesis of the NiAl-LDHs Precursor and Ni_xP_y/Al_2O_3. *Synthesis of Hierarchical NiAl-LDHs Precursor.* NiAl-LDH precursor with molar ratio of $[Ni^{2+}]/[Al^{3+}]$ = 2/1 was synthesized by a urea decomposition method reported by our group previously.[12] Generally, $Ni(NO_3)_2{\cdot}6H_2O$, $Al(NO_3)_3{\cdot}9H_2O$, urea, and NH_4F were dissolved in 100 mL of deionized water to give a transparent solution with the concentration of 0.05 M, 0.025 M, 0.5 and 0.2 M, respectively. The resulting solution was aged in a sealed-Teflon autoclave at 110 °C for 20 h. The obtained precipitation was washed thoroughly with water and dried in an oven at 60 °C overnight.

Synthesis of Ni_xP_y/Al_2O_3. Various supported Ni_xP_y/Al_2O_3 were obtained via an in situ reduction process of the NiAl-LDH followed by a calcination with certain amount of red phosphorus in reducing atmosphere. In the first step, 0.5 g of NiAl-LDH was reduced in a H_2/N_2 (50/50, v/v) stream at 450 °C for 5 h, with a heating rate of 2 °C/min. This reduction process results in the phase transformation of the NiAl-LDH to Ni/Al_2O_3 (Ni loading: ∼ 60 wt %). The resulting product was slowly cooled to the room temperature in a N_2 stream for subsequent synthesis of Ni_xP_y samples. In the second step, 0.05 g of the as-obtained Ni/Al_2O_3 (0.6 mmol Ni) and red phosphorus with different initial Ni/P molar ratios of 2/1, 1/2 and 12/5, respectively, were sealed separately in the two ends of a quartz tube, followed by calcination in a H_2/N_2 (50/50, v/v) stream to produce supported Ni_xP_y samples. Ni_2P and NiP_2 were prepared at 500 °C for 5 h, with an initial heating rate of 2 °C/min; while $Ni_{12}P_5$ was obtained at 800 °C for 4 h, with an initial heating rate of 5 °C/min. The resulting product was slowly cooled to room temperature in a N_2 stream for the subsequent catalytic evaluation.

2.3. Catalytic Evaluation for the Selective Hydrogenation of Phenylacetylene. In a typical reaction, the catalyst (0.55 mmol of Ni), phenylacetylene (1 mL), and 2-propanol solvent (30 mL) were placed into a stainless steel reaction reactor, which was fitted inside a Teflon tank. The air in the vessel was replaced by H_2 three times with a pressure of 2 MPa, vented, and sealed. After the reactor temperature was increased to the target temperature (e.g., 100 °C), H_2 was introduced into the reactor with an initial pressure of 0.3 MPa. After a given reaction time, the reaction product was analyzed off-line by using GC (Shimadzu GC-2014C equipped with a flame ionization detector).

2.4. Characterization. Powder XRD measurements were performed on a Rigaku XRD-6000 diffractometer, using Cu Kα radiation (λ = 0.15418 nm) at 40 kV, 40 mA, with a scanning rate of 5°/min, and a 2θ angle ranging from 3° to 90°. The morphology of the samples was investigated using a Zeiss Supra 55 scanning electron microscope (SEM) with an accelerating voltage of 20 kV, combined with energy dispersive X-ray spectroscopy (EDS) for the determination of metal composition. Transmission electron microscopy (TEM) images were recorded with JEOL JEM-2010 high-resolution transmission electron microscopes. The accelerating voltage was 200 kV. The Ni XAFS measurements were performed at the beamline 1W1B of the Beijing Synchrotron Radiation Facility (BSRF), Institute of High Energy Physics (IHEP), Chinese Academy of Sciences (CAS). Extended X-ray absorption fine structure spectra (EXAFS) were recorded at ambient temperature in transmission mode. The typical energy of the storage ring was 2.5 GeV with a maximum current of 250 mA; the Si (111) double crystal monochromator was used. Fourier transform of the EXAFS spectra was carried out in a K-range from 3.0 to 12.8 $Å^{-1}$. The IFFEFIT 1.2.11 date analysis package (Athena, Artemis, Atoms, and FEFF6) was used for the date analysis and fitting. X-ray photoelectron spectra (XPS) were recorded on a Thermo VG Escalab 250 X-ray photoelectron spectrometer operated at a pressure of 2×10^{-9} Pa using monochromatized Al Kα radiation (1486.6 eV) with a beam diameter of 100 μm. Binding energies were determined with adventitious carbon (C 1s at 284.6 eV) as the reference.

The in situ IR experiment for the adsorption of probe molecule CO and the hydrogenation of acetylene was performed over Bruker infrared spectrometer with the Transmission cell. The IR cell was equipped with KBr windows, connections for inlet and outlet flows, and thermocouples to monitor and control the temperature. The samples (15 mg) were pressed into self-supporting wafers with a diameter of 12 mm. In a general way, the sample was first refreshed in the cell with H_2 at 450 °C for 1.5 h. For the CO IR measurements, the sample after pretreatment was cooled to room temperature in a H_2 flow for the measurement of the primitive reference infrared signal. After 1% CO/N_2 was introduced and purged, the formal infrared signal was collected vs the reference signal. For the hydrogenation IR spectra of acetylene, the sample after pretreatment was cooled to 373 K in a H_2 flow, and then 5% C_2H_2/N_2 was introduced and purged in N_2 flow to remove the gaseous and weakly adsorbed acetylene. The spectra of hydrogenation process were measured at every minute after introducing H_2 at a flow rate of 100 cm^3 min^{-1}.

Hydrogen temperature-programmed desorption (H_2-TPD) measurements were conducted in a quartz tube reactor on a Micromeritics ChemiSorb 2720 with a thermal conductivity detector (TCD). In a typical process, the sample (50 mg) was first sealed and reduced in the reactor in a gaseous mixture of H_2 and Ar (1:9, v/v) at 450 °C for 3 h. Subsequently, the reduced sample was purged in Ar at 450 °C for 30 min, then

DOI: 10.1021/acscatal.5b01429
ACS Catal. 2015, 5, 5756−5765

cooled down to 25 °C for readsorption of H_2; finally the temperature was raised to 500 °C at a heating rate of 10 °C/min in Ar atmosphere.

The CO chemisorption was performed in an Automated Catalyst Characterization System (Autochem 2920) from MICROMERITICS equipped with a thermal conductivity detector (TCD). The sample was first reduced at 400 °C for 1 h followed by cooling to room temperature in a He flow of 50 mL/min. The CO chemisorption was measured at 20 °C by introducing pulses of 5% CO-He flow (50 mL/min) until adsorption saturation. The dispersion of Ni was calculated on the basis of the volume of chemisorbed CO using the following equation:

$$D\% = \frac{V_{ad} \times M_{Ni} \times SF}{m_s \times P \times V_m \times d_r} \times 100 \quad (1)$$

The average particle diameter based on metal dispersion was calculated assuming spherical particles by using the following equation:

$$d = \frac{3 \times M_{Ni} \times F}{N_A \times D \times \rho_{Ni} \times \sigma} \quad (2)$$

where m_s denotes the weight of sample (g); P is the weight fraction of Ni in the sample; V_m is the molar volume of CO at standard temperature and pressure (STP); d_r is the reduction degree of Ni; V_{ad} (mL) is the volume of chemisorbed CO; M_{Ni} is the molecular weight of Ni (58.7 g mol^{-1}); SF is the stoichiometric factor (Ni:CO molar ratio in the chemisorption) which is taken as 1; ρ_{Ni} is the metal density of Ni; D is the dispersion of Ni calculated in eq 1; N_A is Avogadro's number; σ is the atomic cross-sectional area (0.0649 nm^2); and F is the calibration factor.

3. COMPUTATIONAL METHODS

The density functional theory calculations were performed with the Vienna Ab-initio Simulation Package (VASP)[13] in slab models. The single crystal cell structural models for $Ni_{12}P_5$, Ni_2P, and NiP_2 were built according to the XRD standard cards, in which the crystal structure is the same with our experimental results: Ni, F m-3m (225); $Ni_{12}P_5$, I 4/m (87); Ni_2P, P 321 (150); NiP_2, P a-3 (205) (see details in Figure S6). The generalized gradient approximation (GGA) with the Perdew–Burke–Ernzerhof (PBE) functional, and the projector augmented wave (PAW) method were utilized for the geometric optimization and energy calculations. A 1 × 1 × 1 k-point sampling in the surface Brillouin zone was used in the calculations. The vacuum was set to be 20 Å to depress the interaction between adjacent slabs. An energy cutoff of 500 eV and the converge criteria of the force on each relaxed atom below 0.05 eV/Å were used in this work. The desorption energy is defined as follows: $E_d = (E_g + E_{slab}) - E_{total}$, where E_{total} is the energy of the system after adsorption; E_g denotes the energy of the gas phase ethylene, and E_{slab} is the energy of slab before adsorption.

4. RESULTS AND DISCUSSION

4.1. Structural and Morphological Characterization of Ni_xP_y/Al_2O_3. The XRD pattern of NiAl-LDH precursor (Figure S1) shows characteristic reflections at 2θ 11.68°, 23.44°, and 35.10°, which can be indexed to (003), (006), and (012) of an LDH phase, respectively. SEM image (Figure S1, inset) displays that the as-synthesized hierarchical NiAl-LDH is composed of numerous frizzy nanoflakes intercrossing with each other. After an in situ reduction process, the structural topotactic transformation of NiAl-LDH occurs, resulting in the supported Ni/Al_2O_3 sample (Figure 1a) according to the XRD standard

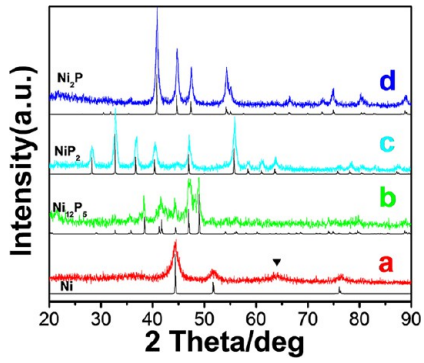

Figure 1. XRD patterns of (a) Ni/Al_2O_3 and Ni_xP_y/Al_2O_3 derived from Ni_2Al-LDH precursor with various ratios of x(Ni):y(P): (b) $Ni_{12}P_5/Al_2O_3$, (c) NiP_2/Al_2O_3, (d) Ni_2P/Al_2O_3. The DFT-simulated XRD patterns for corresponding Ni and Ni_xP_y phase are shown in the lower part of the panels.

card (Ni-PDF#04-0850). A small peak at 2θ 62.85° is indexed to the (110) reflection of NiO phase (NiO-PDF#44-1159) owing to the inevitable partial oxidation of Ni particles exposed to air. Three kinds of nickel phosphides are further obtained by annealing the Ni/Al_2O_3 sample with certain amount of red phosphorus, which can be indexed to $Ni_{12}P_5/Al_2O_3$, Ni_2P/Al_2O_3 and NiP_2/Al_2O_3, respectively (XRD standard cards: $Ni_{12}P_5$-PDF#22-1190; NiP_2-PDF#21-0590; Ni_2P-PDF#03-0953). The corresponding DFT simulated XRD patterns are shown below the measured ones and are consistent with the experimental results (Figure 1). SEM images in Figure2 show that the morphology of all the resulting products (Ni/Al_2O_3, $Ni_{12}P_5/Al_2O_3$, Ni_2P/Al_2O_3, and NiP_2/Al_2O_3) remain the original hierarchical morphology of NiAl-LDH precursor. The corresponding EDS analysis detects the existence of P species in the three Ni_xP_y/Al_2O_3 samples (Figure S2B, 2C, 2D). No obvious agglomeration is observed after the in situ reduction and annealing process, owing to the self-supporting 3D feature of the LDH precursor.

TEM and HRTEM (Figure 3) images further reveal the particular structure of the supported Ni/Al_2O_3 and Ni_xP_y/Al_2O_3. It is observed that Ni nanoparticles are highly dispersed within Al_2O_3 matrix with a mean size of 5.3 nm (Figure 3A1). After further reaction with red phosphorus, the resulting three Ni_xP_y/Al_2O_3 samples also display uniform dispersion. It is found that the mean particle size of $Ni_{12}P_5$ (11.4 nm) is remarkably larger than Ni (5.3 nm), Ni_2P (5.6 nm), and NiP_2 (5.9 nm), which is possibly due to the high preparation temperature. We have also carried out CO chemisorption measurements, so as to provide more evidence for the dispersion of Ni and Ni_xP_y catalysts. The average crystallite size of Ni/Al_2O_3 and Ni_xP_y/Al_2O_3 measured by TEM and CO chemisorption are listed in Table S1. The mean particle sizes measured by CO chemisorption are 6.2 nm (Ni/Al_2O_3), 14.9 nm ($Ni_{12}P_5/Al_2O_3$), 8.8 nm (Ni_2P/Al_2O_3), and 8.5 nm (NiP_2/Al_2O_3), respectively, slightly larger than the TEM results. This is attributed to the following reason: CO is both linear and multicoordinated adsorbed on nickel, whereas the calculation of Ni particle size is based on the assumption that one CO

DOI: 10.1021/acscatal.5b01429
ACS Catal. 2015, 5, 5756–5765

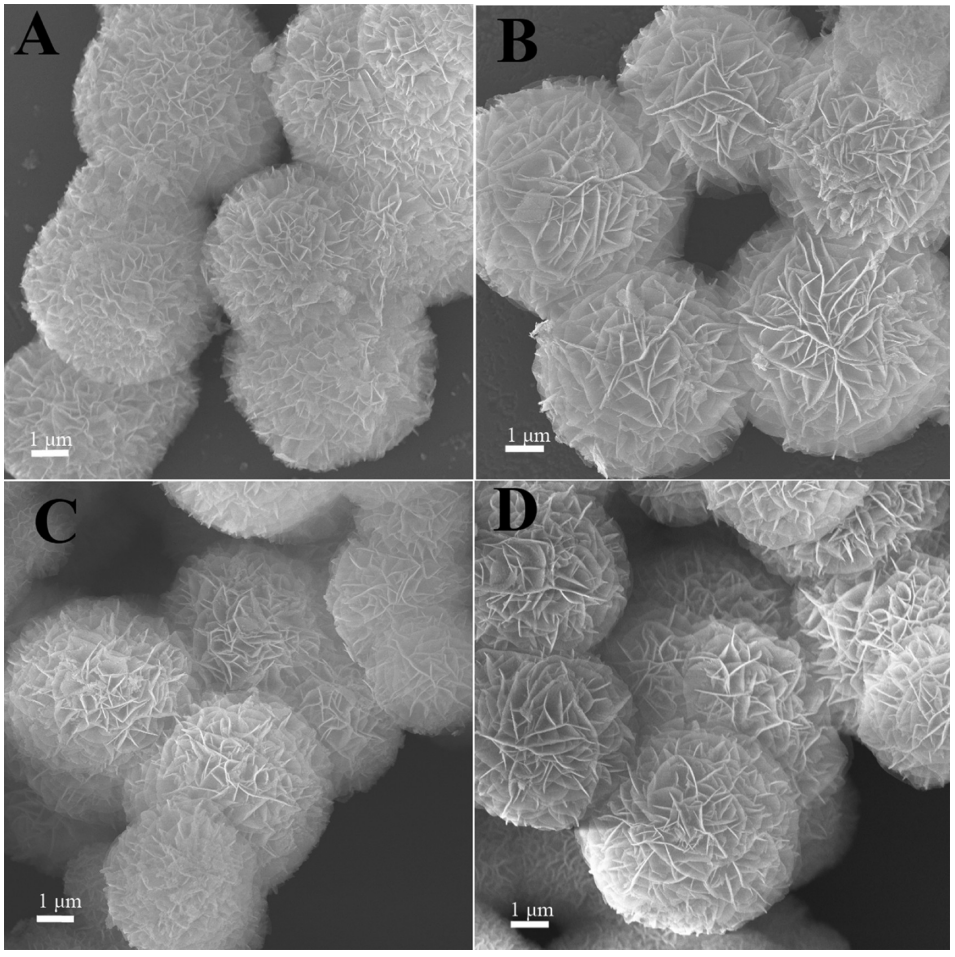

Figure 2. SEM images of (A) Ni/Al_2O_3, (B) $Ni_{12}P_5/Al_2O_3$, (C) Ni_2P/Al_2O_3, (D) NiP_2/Al_2O_3.

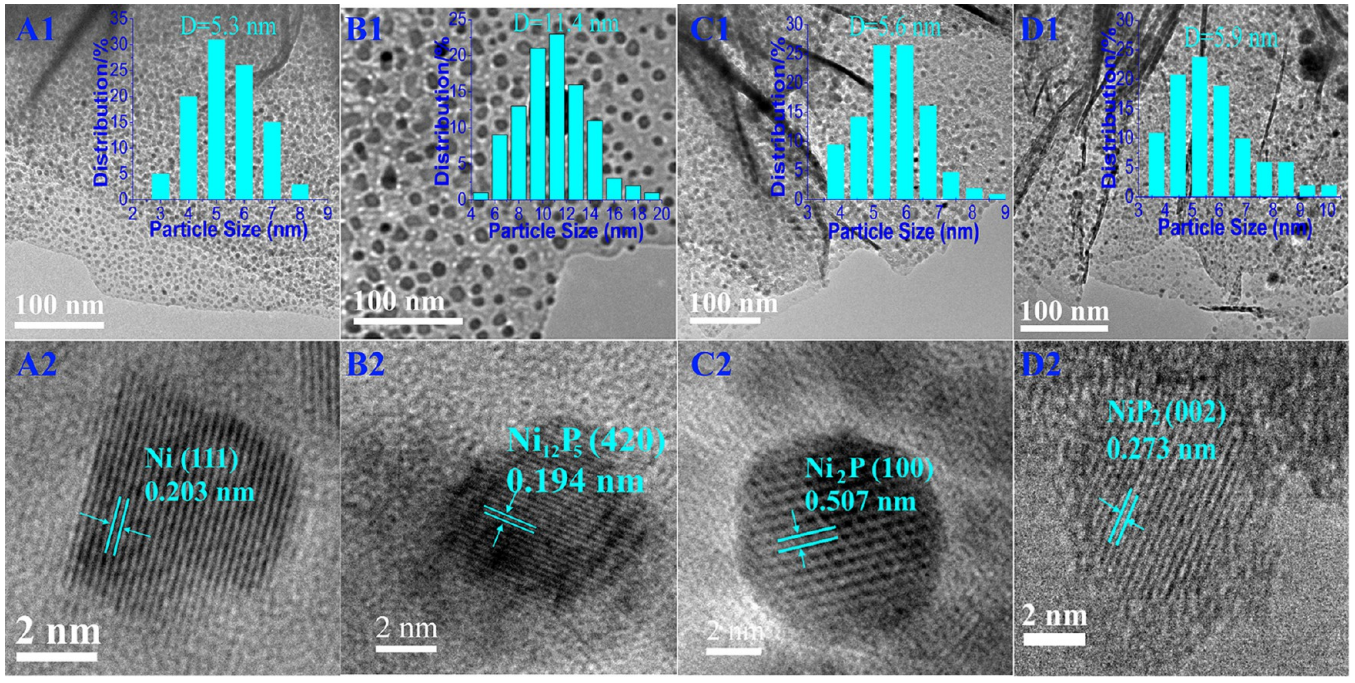

Figure 3. TEM images of (A1) Ni/Al_2O_3, (B1) $Ni_{12}P_5/Al_2O_3$, (C1) Ni_2P/Al_2O_3, (D1) NiP_2/Al_2O_3. The inset shows the size distribution for these Ni_xP_y nanoparticles. The corresponding HRTEM lattice fringe images are shown in A2, B2, C2, and D2, respectively.

DOI: 10.1021/acscatal.5b01429
ACS Catal. 2015, 5, 5756−5765

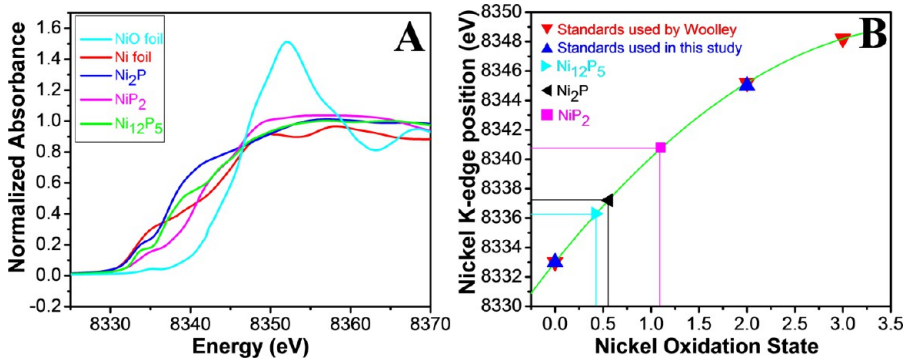

Figure 4. (A) Normalized intensity of Ni K-edge XANES spectra of the Ni_xP_y samples, with Ni foil and NiO as references. (B) Ni K-edge position plotted against Ni oxidation state. Ni K-edge position reported by Woolley et al.[17a] is referred to the position of maximum first derivative for Ni(0) foil, Ni(II)O, and $LaNi(III)O_3$.

molecule is chemisorbed on one Ni surface atom.[14] In addition, the HRTEM images in Figure 3A2, 3B2, 3C2, and 3D2 reveal the lattice fringes of corresponding Ni (d_{111} = 0.203 nm), $Ni_{12}P_5$ (d_{420} = 0.194 nm), Ni_2P (d_{100} = 0.507 nm), and NiP_2 (d_{002} = 0.273 nm), respectively. These are in good accordance with the XRD result (Figure 1), indicating that the red phosphorus reacts with nickel to produce Ni_xP_y/Al_2O_3 catalysts. In addition, this method is extended to the preparation of CoP/Al_2O_3 (Figure S3). We successfully synthesized several kinds of supported and highly dispersed metal phosphides by using the immobilized metal nanoparticles derived from LDHs as "reactive seeds". Owing to the anchoring effect from the support, no obvious sintering/aggregation is found during the reduction and annealing process. Moreover, the chemical composition and structure of the resulting metal phosphides can be facilely tuned.

To better understand the structural features of these supported metal phosphides, X-ray absorption near-edge structure (XANES) spectroscopy was performed to provide electronic structure information, and Fourier transform of Ni K-edge EXAFS was used to illustrate the detailed atomic configuration.[15] The ambient temperature/atmosphere XANES spectra of $Ni_{12}P_5$, Ni_2P, NiP_2 and Ni, NiO references are displayed in Figure 4A. The white line intensities for Ni_xP_y samples are significantly lower than that of NiO reference but closer to Ni foil, indicating that the Ni species in Ni_xP_y samples is mostly reduced.[16] Moreover, it is well-known that the absorbance at the pre-edge feature is sensitive to changes in Ni coordination and symmetry.[16] The Ni_xP_y samples show distinct changes in the pre-edge feature compared with Ni foil, which is likely attributed to the heteroatomic interaction (e.g., intensive Ni−P interaction) and the variations of Ni coordination structure (e.g., the formation of Ni−P coordination). This feature will be further examined in the following R-space spectra. Notably, the K-edge of Ni_xP_y is located between Ni and NiO standard, indicating that the average oxidation state of Ni species in Ni_xP_y ranges in 0−2.[17] Woolley et al.[17a] has reported a nonlinear relationship between nickel oxidation state and K-edge position of Ni(0), Ni(II), and Ni(III) standard. Here, a similar method is used to estimate the oxidation states of Ni_xP_y. Figure 4B and Table S2 show the measured edge positions for the five samples presented in Figure 4A. It is found that the Ni(0) and (II) standard data that we used fit well with those employed by Woolley et al.[17a] Therefore, it is reasonable to use the polynomial best fit line to estimate the oxidation states of Ni_xP_y, with the values of 0.43, 0.56, and 1.1 for $Ni_{12}P_5$, Ni_2P, and NiP_2, respectively. The error in the Ni K-edge position is estimated at ±0.2 eV.

The Fourier transform of Ni K-edge EXAFS oscillations was further used to study the detailed atomic configuration for these Ni_xP_y samples (Figure 5). In the R-space spectra, two

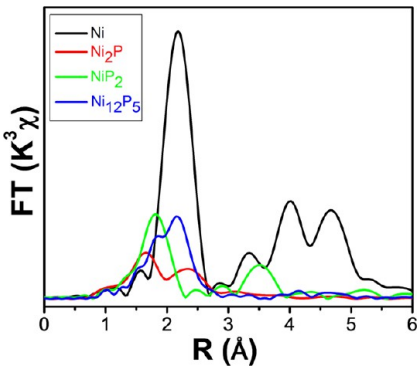

Figure 5. Fourier transform k^3-weighted EXAFS spectra in R space for $Ni_{12}P_5$, Ni_2P and NiP_2 samples, with Ni foil as the reference sample.

coordination shells of Ni_2P centered at ∼0.175 and 0.240 nm are observed, corresponding to Ni−P and Ni−Ni contributions, respectively.[18] With the increase of P/Ni ratio, the peak intensity of Ni−Ni bond decreases significantly accompanying with a peak shift to high R value, indicating a largely reduced Ni−Ni bonding as a result of the separation effect by P element. The peak splitting demonstrates different crystal textures: new bond (e.g., Ni−P coordination) appears in these Ni_xP_y compared with pristine Ni crystal, which agrees well with the results of XRD (Figure 1). In addition, curve-fitting results in Table 1 provide a quantitative analysis of coordination environment in these Ni_xP_y samples. The Ni−Ni bond length increases gradually from Ni foil (2.480 Å) to $Ni_{12}P_5$ (2.520 Å) and then to Ni_2P (2.638 Å); however, no Ni−Ni bond can be detected in the sample of NiP_2. With the enhancement of P/Ni ratio, the coordination number of Ni−Ni bond decreases from 12 (Ni foil) to 1.7 (Ni_2P) and finally disappears in NiP_2. However, the coordination number of Ni−P bond increases from 0 (Ni foil) to 6 (NiP_2), which displays an opposite trend. Moreover, the experimental coordination number of Ni−Ni for Ni_2P (1.7) is much smaller than that of the theoretical value (4). This can be attributed to the highly dispersed nanostructure with very small particle size (5.6 nm) (confirmed by XRD, HRTEM, and CO pulse chemisorption) for the as-

DOI: 10.1021/acscatal.5b01429
ACS Catal. 2015, 5, 5756−5765

Table 1. Curve Fitting Results of Ni K-Edge EXAFS of Ni foil, $Ni_{12}P_5$, Ni_2P, and NiP_2 Samples

sample	shell	R (Å)[a]	CN[b] theoretical value	CN[b] experimental value	$\Delta\sigma^2$ (Å)[c]
Ni foil	Ni−Ni	2.480	12	12	0.0053
$Ni_{12}P_5$	Ni−Ni	2.520	6	5.4	0.0093
	Ni−P	2.241	4	3.1	0.0087
Ni_2P	Ni−Ni	2.638	4	1.7	0.0053
	Ni−P	2.239	6	6.3	0.0125
NiP_2	Ni−P	2.263	6	6	0.0058

[a]Distance between absorber and backscatter atoms. [b]Coordination number. [c]Change in the Debye−Waller factor value relative to the reference sample.

prepared Ni_2P sample. It has been reported that smaller Ni_2P crystallites show stronger Ni−P interactions and extra exposure of phosphorus on the surface, which intend to produce a larger Ni−P coordination number and significant decrease of Ni−Ni coordination, in comparison with the Ni_2P bulk phase or theoretical value.[19] The results above demonstrate that the Ni atoms are gradually dispersed by P atoms, indicative of the geometric effect in these Ni_xP_y samples.

XPS measurements were carried out to give information on the electronic structure of Ni_xP_y samples (Figure S4). The Ni $2p_{3/2}$ core level spectrum of Ni/Al_2O_3 (Figure S4A, sample a: ~856.3 eV) can be divided into two subpeaks centered at 855.8 and 857.5 eV, respectively, which are attributed to Ni^{2+} in NiO and Ni^{2+} in surface $NiAl_2O_4$ spinel.[20] Moreover, a broad shakeup satellite signal (at ~862.5 eV) is observed.[20] In the cases of $Ni_{12}P_5$, Ni_2P and NiP_2 samples (Figure S4A, samples b−d), the Ni $2p_{3/2}$ signal shows an additional weak peak located at ~853.0 eV, which can be assigned to $Ni^{\delta+}$ species. Similarly, the $2p_{3/2}$ signal of red phosphorus (Figure S4B, sample a, blue line) shows two peaks at binding energies of 129.6 and 134.3 eV, which can be attributed to elemental phosphorus (P^0) and oxidized/passivated phosphorus, respectively.[5a,20d,21] Notably, it is found that the peak of P $2p_{3/2}$ assigned to elemental phosphorus (nonoxidated P) in Ni_xP_y shifts to lower binding energy relative to red phosphorus (129.6 eV) (Figure S4B, samples b−d, blue lines), indicating the existence of $P^{\delta-}$. The results above demonstrate an electronic interaction, in which electron transfer occurs from Ni to P in these Ni_xP_y samples.

4.2. Catalytic Evaluation of Ni_xP_y and Structure−Property Correlation Study. The selective hydrogenation of phenylacetylene was used as a model reaction to evaluate the catalytic behavior of supported Ni_xP_y/Al_2O_3, with Ni/Al_2O_3 and Ni_2P/γ-Al_2O_3 as reference samples. Figure 6 illustrates the catalytic conversion and corresponding selectivity toward hydrogenation of phenylacetylene over these catalysts vs reaction time. It is observed that the monometallic Ni/Al_2O_3 catalyst shows the best hydrogenation activity but the worst selectivity (Figure 6, curve a). The catalytic activity decreases gradually along with the increase of P/Ni ratio for these supported Ni_xP_y/Al_2O_3 samples, with the following sequence: Ni > $Ni_{12}P_5$ > Ni_2P > NiP_2 (Figure 6A, curves a−d). However, with the gradual incorporation of P, the selectivity toward styrene enhances dramatically from 0.7% (Ni/Al_2O_3) to 48.0% ($Ni_{12}P_5/Al_2O_3$) and then to the maximum 88.2% (Ni_2P/Al_2O_3), followed by a decrease to 65.9% (NiP_2/Al_2O_3) (Figure 6B, curves a−d). The sample of Ni_2P/Al_2O_3 exhibits the best

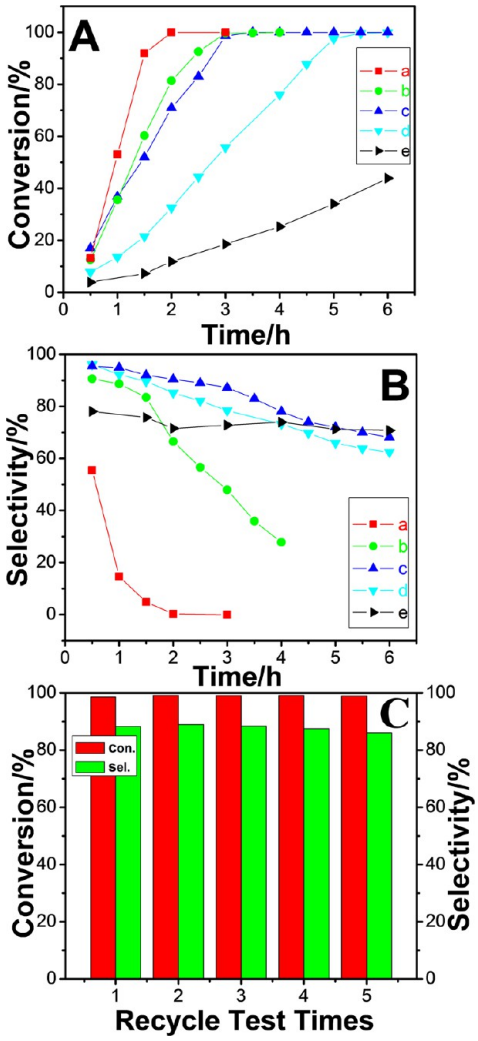

Figure 6. Catalytic conversion (A) and corresponding selectivity (B) vs reaction time for the hydrogenation of phenylacetylene to styrene over various catalysts: (a) Ni/Al_2O_3, (b) $Ni_{12}P_5/Al_2O_3$, (c) Ni_2P/Al_2O_3, (d) NiP_2/Al_2O_3, (e) Ni_2P/γ-Al_2O_3 (prepared by impregnation method). (C) The catalytic conversion and corresponding selectivity vs recycling times over Ni_2P/Al_2O_3 catalyst. Reaction conditions: phenylacetylene/Ni = 16.5 (Ni: 0.55 mmol); phenylacetylene: 1.0 mL; iso-PrOH: 30 mL; temperature: 100 °C; H_2 pressure: 0.3 MPa.

catalytic performance with the conversion of 98.6% and selectivity of 88.2% (100 °C, 0.3 MPa, 3 h). The Ni_2P/γ-Al_2O_3 catalyst was prepared via the conventional impregnation method as a reference sample, with the mean particle size of 62.8 nm (Figure S7). It can be seen from Figure 6 that both the activity and selectivity of Ni_2P/Al_2O_3 catalyst (98.6%, 88.2%) are much better than those of Ni_2P/γ-Al_2O_3 (43.9%, 70.8%).

The stability of Ni_2P/Al_2O_3 catalyst was investigated by recycling for five times under the same condition. The conversion of phenylacetylene and selectivity toward styrene (100 °C; H_2 pressure: 0.3 MPa; 3 h) over Ni_2P/Al_2O_3 catalyst are shown in Figure 6C. The conversion still remains above 98%, and a slight decrease in selectivity is found (from 88.2% to 86.1%) after 5 recycles. The results show a satisfactory stability and reusability of the Ni_2P/Al_2O_3 catalyst.

In heterogeneous catalysis, the catalytic reactions occur mainly at the catalyst surface, and IR spectroscopy of CO chemisorption is an excellent method to probe the surface

DOI: 10.1021/acscatal.5b01429
ACS Catal. 2015, 5, 5756−5765

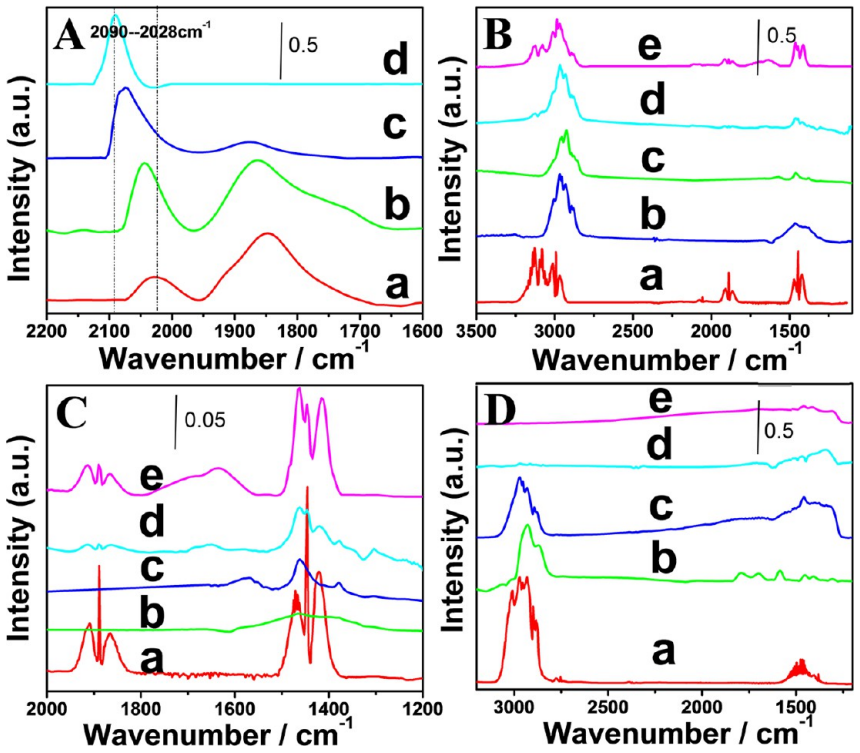

Figure 7. (A) In situ Fourier-transformed infrared spectra of CO adsorption on (a) Ni/Al_2O_3, (b) $Ni_{12}P_5/Al_2O_3$, (c) Ni_2P/Al_2O_3, (d) NiP_2/Al_2O_3; (B) the standard spectrum of ethylene (a) and the in situ Fourier-transformed infrared spectra of the hydrogenation progress of acetylene over (b) Ni, (c) $Ni_{12}P_5$, (d) Ni_2P, (e) NiP_2; (C) magnified signal of the wavenumber region where the ν(C═C) and δ(═C−H) appear in (B) (a) ethylene, and intermediates over (b) Ni, (c) $Ni_{12}P_5$, (d) Ni_2P, (e) NiP_2; (D) the standard spectrum of ethane (a) and the in situ Fourier-transformed infrared spectra of the desorption progress of ethylene over (b) Ni, (c) $Ni_{12}P_5$, (d) Ni_2P, (e) NiP_2.

structure of catalysts.[20,22] The in situ Fourier-transformed infrared absorption of CO molecule over Ni_xP_y samples was performed, in comparison with the monometallic Ni sample (Figure 7A). Normally, CO adsorbs on Ni catalysts with two modes, namely, linear (above 2000 cm^{-1}) and multicoordinated adsorption (below 2000 cm^{-1});[18b,23] while CO adsorption onto P surface is too weak to be detected at room temperature. For monometallic Ni/Al_2O_3 catalyst (Figure 7A-a), both the linear adsorption at 2028 cm^{-1} and multicoordinated adsorption at 1848 cm^{-1} are observed, respectively. With the increase of P/Ni ratio in these Ni_xP_y samples, the linear adsorption peak enhances gradually while the multicoordinated adsorption peak decreases dramatically and finally disappears (Figure 7A-b, 7A-c and 7A-d). Moreover, the linear adsorption peak undergoes a blue shift (~62 cm^{-1}) from Ni/Al_2O_3 to NiP_2/Al_2O_3. Generally, changes in the CO adsorption properties can be explained by two aspects: electronic effect and geometric effect.[24] The blue shift (~62 cm^{-1}) of linear adsorption peak corresponds to a positively charged Ni; the reduced electron density of Ni ($Ni^{\delta+}$) decreases the d-π electron feedback from metal Ni to antibonding orbital (π^*) of adsorbed CO molecule, resulting in the gradual blue shift of linear CO adsorption. With respect to the geometric effect,[18b,25] the addition of P component separates the continuous Ni sites and increases the Ni−Ni bond length in the cases of Ni_2P and NiP_2 samples, which leads to the significantly depressed CO multiadsorption. Herein, the electronic and geometry feature are clearly demonstrated by XAFS, XPS, and in situ CO IR for these Ni_xP_y catalysts, which are useful to understand their unique catalytic properties for hydrogenation.

For hydrogenation reaction over transition metal catalysts, they normally obey the Horiuti−Polanyi mechanism, which involves hydrogen molecule dissociation followed by the sequential addition of atomic hydrogen to the substrate.[26] The H_2-TPD measurements over Ni and Ni_xP_y samples (Figure S5) were performed to characterize the hydrogen adsorption ability of these heterogeneous catalysts. For monometallic Ni catalyst (Figure S5, curve a), a strong desorption peak at 150 °C is observed, which can be assigned to the hollow sites for the most energetically favorable adsorption confirmed by DFT studies.[27] For Ni_xP_y catalysts (Figure S5, curve b, c, d), two desorption peaks at 80 and 125 °C are found; the total integral area decreases gradually along with the increase of P/Ni ratio, indicating the reduction of surface concentration of H atom owing to the decreased Ni sites. Previous studies have proved that the adsorbed hydrogen contributes to the catalytic activity.[28] Therefore, the reduced surface concentration of H atom may account for the gradually decreased reaction activity from Ni to NiP_2.

The in situ IR characterization is an effective technique to provide the information on intermediates, surface-bonding state, and the mechanism pathways of the reaction process.[29] As the hydrogenation reaction occurs on the adsorbed alkyne group, acetylene is used as a probe molecule. Figure 7 shows the hydrogenation and desorption IR spectra of acetylene over Ni/Al_2O_3 and Ni_xP_y/Al_2O_3. For the hydrogenation process shown in Figure 7B, the standard spectra of ethylene is shown in Figure 7B-a, the intensity of ν(═C−H) at 3124−3075 cm^{-1} and δ(═C−H) at 1471−1421 cm^{-1} increases with the enhancement of P/Ni ratio. In the cases of Ni_2P and NiP_2 (Figure 7C-d and 7C-e), the characteristic peaks of ν(C═C) at

DOI: 10.1021/acscatal.5b01429
ACS Catal. 2015, 5, 5756−5765

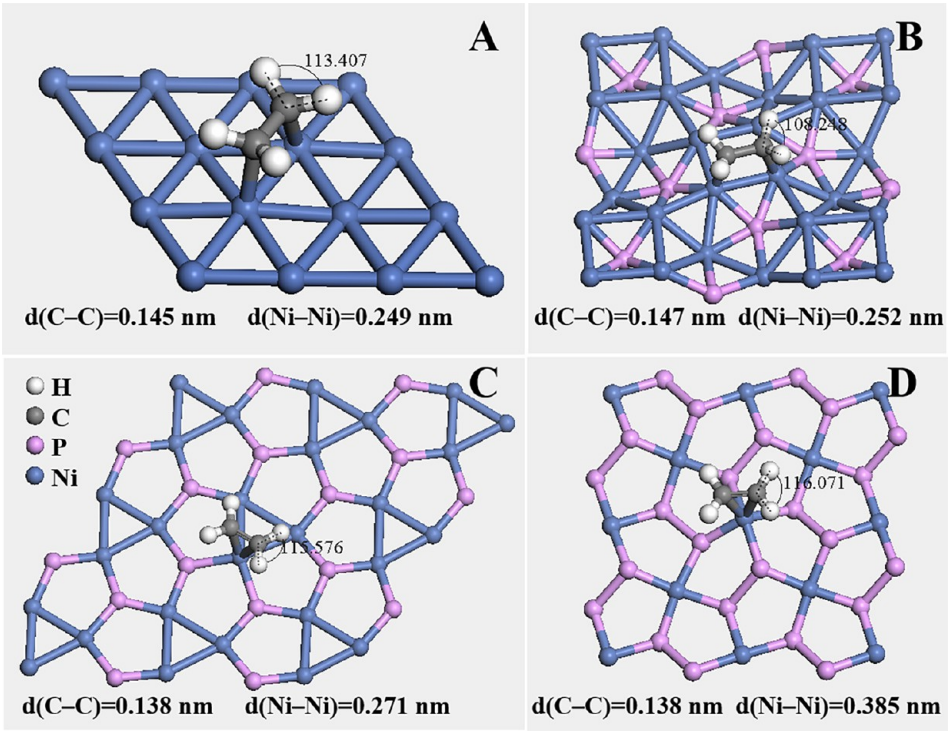

Figure 8. Atomic arrangement and chemical bonding of the preferential crystal face of Ni and Ni_xP_y (according to HRTEM): (A) Ni (111) face, (B) $Ni_{12}P_5$ (001) face, (C) Ni_2P (001) face, (D) NiP_2 (001) face.

1909−1865 cm^{-1} are clearly observed, which are not detected over Ni and $Ni_{12}P_5$ catalyst (Figure 7C-b and 7C-c). This indicates that selective hydrogenation of acetylene to ethylene occurs over Ni_2P and NiP_2; while deep hydrogenation to ethane occurs over Ni and $Ni_{12}P_5$. For the desorption process (Figure 7D), the acetylene completely converts to ethane (Figure 7D-a) over Ni and $Ni_{12}P_5$ (Figure 7D-b and 7D-c) while the intermediate ethylene desorbs from the surface of Ni_2P and NiP_2 (Figure 7D-d and 7D-e) before its further hydrogenation. According to previous research,[30] this might be due to the reason that the desorption energy is less than the activation barrier for further hydrogenation over the Ni_2P and NiP_2 samples.

DFT calculations were further performed to give a deep understanding on the electron and geometry features of Ni_xP_y. It has been reported that the (001) facet of Ni_2P is the most stable surface demonstrated by both experimental[31] and DFT studies.[5c] For a comparison study, we choose the (001) facet of these three Ni_xP_y for the DFT calculations. The structural models of Ni and Ni_xP_y are built according to their XRD patterns (Figure S6). Robert Schlögl et al.[25] have reported the so-called "active-site isolation" theory for traditional alloy catalysts, in which the active metal can be uniformly dispersed and isolated at atomic level by the second inert metal. For nickel phosphides in this work, the isolation of active Ni by inactive P is clearly seen in Figure 8. For Ni crystal, each Ni atom is surrounded and coordinated by other Ni atoms. With the increase of P/Ni ratio, the Ni−Ni coordination decreases gradually while the Ni−P coordination increases. No Ni−Ni coordination is observed in the case of NiP_2 sample (Figure 8D). The results agree well with the curve-fitting EXAFS data (Table 1).

The introduction of P in Ni_xP_y significantly changes the geometric construction of active Ni sites, which would impose great impact on the adsorption and hydrogenation of C═C bond. Figure 8 also displays the optimum adsorption state of ethylene over Ni and Ni_xP_y. The distance of the carbon−carbon bond of the adsorbed intermediate and the bond angle over Ni (0.145 nm, 113.4°) and $Ni_{12}P_5$ (0.147 nm, 108.3°) are close to ethane (0.154 nm, 109.5°), indicating that the double bond and the orbital hybridization of carbon change from sp^2 to sp^3, so as to form di-σ(CC) adsorption. This leads to further hydrogenation to ethane easily, accounting for the poor selectivity. For Ni_2P catalyst, however, the length of the C−C bond is 0.138 nm, and the bond angle is 115.6°, which are close to ethylene (0.133 nm, 120°), indicating that the double bond remains undissociated. Although Ni_2P still has three consecutive Ni atoms, the distance of Ni−Ni is 0.271 nm (a little larger than the EXAFS result 0.264 nm), which is too long to induce the orbital hybridization of carbon carbon double bond from sp^2 to sp^3 for the formation of dissociated di-σ(CC) adsorption. Therefore, orbital hybridization of the double bond intermediate still keeps unchanged sp^2 and forms di-π(C═C) adsorption on a single nickel. For the sample of NiP_2, every Ni is surrounded by four P; the distance of adjacent Ni is 0.385 nm, which is too far to form Ni−Ni bond. As a result, the adsorption state is similar to Ni_2P.

Once ethylene is formed on the catalyst surface, it can desorb or react further; the latter outcome will lead to the unwanted formation of ethane. Ethylene from the gas phase can also adsorb on the surface and has the same possibility of further hydrogenation to ethane.[13,30] It is known that the selectivity is determined by both the desorption energy of ethylene (E_d) and its activation barrier of further hydrogenation (E_a). A selective catalyst should possess a less barrier for ethylene desorption than the activation barrier for the ethylene hydrogenation. In order to give a detailed understanding on the catalytic selectivity for these Ni_xP_y samples, both of the two parameters

DOI: 10.1021/acscatal.5b01429
ACS Catal. 2015, 5, 5756−5765

over $Ni_{12}P_5$, Ni_2P, and NiP_2 were calculated. The E_d values of ethylene over $Ni_{12}P_5$, Ni_2P, and NiP_2 are +1.764 eV, +1.109 eV and +0.936 eV, respectively, whereas the E_a of further hydrogenation are +2.027 eV, + 2.139 eV and +1.341 eV, respectively. Therefore, ΔE, the energy difference between E_a and E_d ($\Delta E = E_a - E_d$), shows a decrease in the following order: Ni_2P (1.030 eV) > NiP_2 (0.405 eV) > $Ni_{12}P_5$ (0.263 eV). This is in good accordance with the results of catalytic selectivity over these three Ni_xP_y samples, accounting for the best selectivity of Ni_2P.

5. CONCLUSIONS

In conclusion, we report the fabrication of several supported nickel phosphides ($Ni_{12}P_5$, Ni_2P and NiP_2) with high dispersion via a two-step procedure based on LDHs approach. The resulting material exhibits largely enhanced catalytic activity and selectivity for hydrogenation of phenylacetylene. The in situ IR of CO adsorption, H_2-TPD, EXAFS, and DFT calculations confirm the isolation effect of Ni active sites by P as well as the charge transfer from Ni to P in these Ni_xP_y catalysts. On the one hand, the increase of Ni−Ni bond length changes the adsorption state of alkene intermediate: when the distance of Ni−Ni bond extends to 0.264 nm, the dissociated di-σ(CC) adsorption converts to di-π(C═C) adsorption, which favors the production of alkene. On the other hand, the reduced electron density of Ni sites ($Ni^{\delta+}$) decreases the desorption energy of alkene, resulting in the enhanced selectivity. Our approach holds significant promise for nickel phosphides as efficient catalysts toward selective hydrogenation of phenylacetylene, and gives a deep insight into the intrinsic structure−property correlation.

■ ASSOCIATED CONTENT

Supporting Information

The Supporting Information is available free of charge on the ACS Publications website at DOI: 10.1021/acscatal.5b01429.

Synthesis protocol and supplemental data, Figures S1−S7 (PDF)

■ AUTHOR INFORMATION

Corresponding Authors

*E-mail: vh30@163.com (S. He).

*E-mail: weimin@mail.buct.edu.cn (M. Wei).

Notes

The authors declare no competing financial interest.

■ ACKNOWLEDGMENTS

This work was supported by the 973 Program (Grant No. 2011CBA00504), the National Natural Science Foundation of China (NSFC), and the Specialized Research Fund for the Doctoral Program of Higher Education (20130010110013). M.W. particularly appreciates the financial aid from the China National Funds for Distinguished Young Scientists of the NSFC. We thank for the support of BSRF (Beijing Synchrotron Radiation Facility) during the XAFS and PAS measurements.

■ REFERENCES

(1) Carenco, S.; Portehault, D.; Boissiere, C.; Mezailles, N.; Sanchez, C. *Chem. Rev.* **2013**, *113*, 7981−8065.

(2) Carenco, S.; Le Goff, X. F.; Shi, J.; Roiban, L.; Ersen, O.; Boissière, C.; Sanchez, C.; Mézailles, N. *Chem. Mater.* **2011**, *23*, 2270−2277.

(3) (a) Hall, J. W.; Membreno, N.; Wu, J.; Celio, H.; Jones, R. A.; Stevenson, K. J. *J. Am. Chem. Soc.* **2012**, *134*, 5532−5535. (b) Popczun, E. J.; McKone, J. R.; Read, C. G.; Biacchi, A. J.; Wiltrout, A. M.; Lewis, N. S.; Schaak, R. E. *J. Am. Chem. Soc.* **2013**, *135*, 9267−9270.

(4) (a) Bowker, R. H.; Smith, M. C.; Pease, M. L.; Slenkamp, K. M.; Kovarik, L.; Bussell, M. E. *ACS Catal.* **2011**, *1*, 917−922. (b) Liang, Y.; Liu, Q.; Asiri, A. M.; Sun, X.; Luo, Y. *ACS Catal.* **2014**, *4*, 4065−4069. (c) Xing, Z.; Liu, Q.; Asiri, A. M.; Sun, X. *ACS Catal.* **2014**, *5*, 145−149. (d) Wei, J. D.; Ni, Y. H.; Xiang, N. N.; Zhang, Y. X.; Ma, X. *CrystEngComm* **2014**, *16*, 2113−2118. (e) Soni, K. K.; Boahene, P. E.; Rambabu, N.; Dalai, A. K.; Adjaye, J. *Catal. Today* **2013**, *207*, 119−126. (f) Hayes, J. R.; Bowker, R. H.; Gaudette, A. F.; Smith, M. C.; Moak, C. E.; Nam, C. Y.; Pratum, T. K.; Bussell, M. E. *J. Catal.* **2010**, *276*, 249−258.

(5) (a) Bui, P.; Cecilia, J.; Oyama, T. S.; Takagaki, A.; Infantes-Molina, A.; Zhao, H.; Li, D.; Rodríguez-Castellón, E.; Jiménez-López, A. *J. Catal.* **2012**, *294*, 184−196. (b) Bando, K. K.; Wada, T.; Miyamoto, T.; Miyazaki, K.; Takakusagi, S.; Koike, Y.; Inada, Y.; Nomura, M.; Yamaguchi, A.; Gott, T.; Oyama, S. T.; Asakura, K. *J. Catal.* **2012**, *286*, 165−171. (c) Prins, R.; Bussell, M. E. *Catal. Lett.* **2012**, *142*, 1413−1436.

(6) Carenco, S.; Leyva-Pérez, A.; Concepción, P.; Boissière, C.; Mézailles, N.; Sanchez, C.; Corma, A. *Nano Today* **2012**, *7*, 21−28.

(7) Barry, B. M.; Gillan, E. G. *Chem. Mater.* **2009**, *21*, 4454−4461.

(8) Carenco, S.; Hu, Y.; Florea, I.; Ersen, O.; Boissière, C.; Mézailles, N.; Sanchez, C. *Chem. Mater.* **2012**, *24*, 4134−4145.

(9) Oyama, S. T.; Gott, T.; Asakura, K.; Takakusagi, S.; Miyazaki, K.; Koike, Y.; Bando, K. K. *J. Catal.* **2009**, *268*, 209−222.

(10) (a) Fan, G. L.; Li, F.; Evans, D. G.; Duan, X. *Chem. Soc. Rev.* **2014**, *43*, 7040−7066. (b) Fogg, A. M.; Rohl, A. L.; Parkinson, G. M.; O'Hare, D. *Chem. Mater.* **1999**, *11*, 1194−1200. (c) Sideris, P. J.; Nielsen, U. G.; Gan, Z. H.; Grey, C. P. *Science* **2008**, *321*, 113−115.

(11) (a) He, Y. F.; Feng, J. T.; Du, Y. Y.; Li, D. Q. *ACS Catal.* **2012**, *2*, 1703−1710. (b) Zhang, F. Z.; Zhao, X. F.; Feng, C.; Li, B.; Chen, T.; Lu, W.; Lei, X. D.; Xu, S. L. *ACS Catal.* **2011**, *1*, 232−237. (c) Zhao, M. Q.; Zhang, Q.; Zhang, W.; Huang, J. Q.; Zhang, Y.; Su, D. S.; Wei, F. *J. Am. Chem. Soc.* **2010**, *132*, 14739−14741. (d) Tian, G. L.; Zhao, M. Q.; Zhang, B.; Zhang, Q.; Zhang, W.; Huang, J. Q.; Chen, T. C.; Qian, W. Z.; Su, D. S.; Wei, F. *J. Mater. Chem. A* **2013**, *2*, 1686−1696.

(12) (a) Li, C. M.; Chen, Y. D.; Zhang, S. T.; Xu, S. M.; Zhou, J. Y.; Wang, F.; Wei, M.; Evans, D. G.; Duan, X. *Chem. Mater.* **2013**, *25*, 3888−3896. (b) Li, C. M.; Chen, Y. D.; Zhang, S. T.; Zhou, J. Y.; Wang, F.; He, S.; Wei, M.; Evans, D. G.; Duan, X. *ChemCatChem* **2014**, *6*, 824−831. (c) He, S.; Li, C. M.; Chen, H.; Su, D. S.; Zhang, B. S.; Cao, X. Z.; Wang, B. Y.; Wei, M.; Evans, D. G.; Duan, X. *Chem. Mater.* **2013**, *25*, 1040−1046.

(13) Yang, B.; Burch, R.; Hardacre, C.; Headdock, G.; Hu, P. *ACS Catal.* **2012**, *2*, 1027−1032.

(14) (a) Geyer, R.; Hunold, J.; Keck, M.; Kraak, P.; Pachulski, A.; Schodel, R. *Chem. Ing. Tech.* **2012**, *84*, 160−164. (b) Zhao, H.; Li, D.; Bui, P.; Oyama, S. *Appl. Catal., A* **2011**, *391*, 305−310.

(15) (a) Hirsch, O.; Zeng, G.; Luo, L.; Staniuk, M.; Abdala, P. M.; van Beek, W.; Rechberger, F.; Süess, M. J.; Niederberger, M.; Koziej, D. *Chem. Mater.* **2014**, *26*, 4505−4513. (b) Oyama, S. T.; Gott, T.; Zhao, H.; Lee, Y.-K. *Catal. Today* **2009**, *143*, 94−107.

(16) Oyama, S. T.; Gott, T.; Asakura, K.; Takakusagi, S.; Miyazaki, K.; Koike, Y.; Bando, K. K. *J. Catal.* **2009**, *268*, 209−222.

(17) (a) Woolley, R. J.; Illy, B. N.; Ryan, M. P.; Skinner, S. J. *J. Mater. Chem.* **2011**, *21*, 18592−18596. (b) Medarde, M.; Dallera, C.; Grioni, M.; Delley, B.; Vernay, F.; Mesot, J.; Sikora, M.; Alonso, J. A.; Martínez-Lope, M. J. *Phys. Rev. B: Condens. Matter Mater. Phys.* **2009**, *80*, 2443−2451.

(18) (a) Moon, J. S.; Kim, E. G.; Lee, Y. K. *J. Catal.* **2014**, *311*, 144−152. (b) Lee, Y.; Oyama, S. *J. Catal.* **2006**, *239*, 376−389. (c) Moreau, L. M.; Ha, D. H.; Zhang, H.; Hovden, R.; Muller, D. A.; Robinson, R. D. *Chem. Mater.* **2013**, *25*, 2394−2403.

(19) (a) Oyama, S. T. *J. Catal.* **2003**, *216*, 343−352. (b) Cho, A.; Takagaki, A.; Kikuchi, R.; Oyama, S. T. *Top. Catal.* **2015**, *58*, 219−231.

DOI: 10.1021/acscatal.5b01429
ACS Catal. 2015, 5, 5756−5765

(20) (a) Cecilia, J. A.; Infantes-Molina, A.; Rodríguez-Castellón, E.; Jiménez-López, A. *J. Catal.* **2009**, *263*, 4−15. (b) Xiao, C.; Liang, M. H.; Gao, A.; Xie, J. L.; Wang, Y.; Liu, H. C. *J. Nanopart. Res.* **2013**, *15*, 98−106. (c) Wang, Y.; Chen, X.; Yue, B.; He, H. *Top. Catal.* **2012**, *55*, 1022−1031. (d) Heracleous, E.; Lee, A. F.; Wilson, K.; Lemonidou, A. A. *J. Catal.* **2005**, *231*, 159−171. (e) Wang, R.; Li, Y.; Shi, R.; Yang, M. *J. Mol. Catal. A: Chem.* **2011**, *344*, 122−127. (f) Hoffer, B. W.; van Langeveld, A. D.; Janssens, J.; Bonné, R.; Lok, C. M.; Moulijn, J. A. *J. Catal.* **2000**, *192*, 432−440.
(21) Blanchard, P. E. R.; Grosvenor, A. P.; Cavell, R. G.; Mar, A. *Chem. Mater.* **2008**, *20*, 7081−7088.
(22) (a) Onda, A.; Komatsu, T.; Yashima, T. *J. Catal.* **2004**, *221*, 378−385. (b) Armbrüster, M.; Behrens, M.; Cinquini, F.; Föttinger, K.; Grin, Y.; Haghofer, A.; Klötzer, B.; Knop-Gericke, A.; Lorenz, H.; Ota, A.; Penner, S.; Prinz, J.; Rameshan, C.; Révay, Z.; Rosenthal, D.; Rupprechter, G.; Sautet, P.; Schlögl, R.; Shao, L.; Szentmiklósi, L.; Teschner, D.; Torres, D.; Wagner, R.; Widmer, R.; Wowsnick, G. *ChemCatChem* **2012**, *4*, 1048−1063.
(23) Derrouiche, S.; Bianchi, D. *Appl. Catal., A* **2006**, *313*, 208−217.
(24) (a) He, Y. F.; Liang, L.; Liu, Y.; Feng, J. T.; Ma, C.; Li, D. Q. *J. Catal.* **2014**, *309*, 166−173. (b) Doherty, R. P.; Krafft, J.-M.; Méthivier, C.; Casale, S.; Remita, H.; Louis, C.; Thomas, C. *J. Catal.* **2012**, *287*, 102−113.
(25) Armbrüster, M.; Kovnir, K.; Behrens, M.; Teschner, D.; Grin, Y.; Schlögl, R. *J. Am. Chem. Soc.* **2010**, *132*, 14745−14747.
(26) (a) Horiuti, I.; Polanyi, M. *Trans. Faraday Soc.* **1934**, *30*, 1164−1172. (b) Horiuti, I.; Polanyi, M. *Nature* **1933**, *132*, 819−819. (c) Yang, B.; Gong, X. Q.; Wang, H. F.; Cao, X. M.; Rooney, J. J.; Hu, P. *J. Am. Chem. Soc.* **2013**, *135*, 15244−15250.
(27) (a) Panczyk, T.; Szabelski, P.; Rudzinski, W. *J. Phys. Chem. B* **2005**, *109*, 10986−10994. (b) Monder, D. S.; Karan, K. *J. Phys. Chem. C* **2010**, *114*, 22597−22602.
(28) (a) Lin, W.; Cheng, H.; He, L.; Yu, Y.; Zhao, F. *J. Catal.* **2013**, *303*, 110−116. (b) Liu, Y.; Chen, J.; Zhang, J. *Chin. J. Chem. Eng.* **2007**, *15*, 63−67.
(29) (a) Liu, W.; Arean, C. O.; Bordiga, S.; Groppo, E.; Zecchina, A. *ChemCatChem* **2011**, *3*, 222−226. (b) Beebe, T. P.; Yates, J. T. *J. Am. Chem. Soc.* **1986**, *108*, 663−671.
(30) Studt, F.; Abild-Pedersen, F.; Bligaard, T.; Sørensen, R. Z.; Christensen, C. H.; Nørskov, J. K. *Science* **2008**, *320*, 1320−1322.
(31) (a) Moula, G.; Suzuki, S.; Chun, W.; Otani, S.; Oyama, S.; Asakura, K. *Chem. Lett.* **2006**, *35*, 90−91. (b) Suzuki, S.; Moula, G.; Miyamoto, T.; Nakagawa, Y.; Kinosthita, K.; Asakura, K.; Oyama, S.; Otani, S. *J. Nanosci. Nanotechnol.* **2009**, *9*, 195−201. (c) Hernandez, A.; Ariga, H.; Takakusagi, S.; Kinoshita, K.; Suzuki, S.; Otani, S.; Oyama, S.; Asakura, K. *Chem. Phys. Lett.* **2011**, *513*, 48−52.

DOI: 10.1021/acscatal.5b01429
ACS Catal. 2015, 5, 5756−5765